

PAPER

Robust and Accurate Image Expansion Algorithm Based on Double Scattered Range Points Migration for UWB Imaging Radars

Shouhei KIDERA^{†a)} and Tetsuo KIRIMOTO[†], *Members*

SUMMARY UWB (Ultra Wideband) radar offers great promise for advanced near field sensors due to its high range resolution. In particular, it is suitable for rescue or resource exploration robots, which need to identify a target in low visibility or acoustically harsh environments. Recently, radar algorithms that actively coordinate multiple scattered components have been developed to enhance the imaging range beyond what can be achieved by synthesizing a single scattered component. Although we previously developed an accurate algorithm for imaging shadow regions with low computational complexity using derivatives of observed ranges for double scattered signals, the algorithm yields inaccurate images under the severe interference situations that occur with complex-shaped or multiple objects or in noisy environments. This is because small range fluctuations arising from interference or random noises can produce non-negligible image degradation owing to inaccuracy in the range derivative calculation. As a solution to this difficulty, this paper proposes a novel imaging algorithm that does not use the range derivatives of doubly scattered signals, and instead extracts a feature of expansive distributions of the observed ranges, using a unique property inherent to the doubly scattering mechanism. Numerical simulation examples of complex-shaped or multiple targets are presented to demonstrate the distinct advantage of the proposed algorithm which creates more accurate images even for complicated objects or in noisy situations.

key words: UWB radar, double scattered wave, shadow region imaging, range points migration (RPM)

1. Introduction

UWB pulse radar with high range resolution has versatile applications in near field measurements. One of the most promising applications is a robotic sensor that is able to identify human bodies even in low visibility, such as in dark smog or dusty air in disaster areas or high-density gas in resource exploration situations. Furthermore, it has a potential application in the accurate surface extraction of the human breast in early-stage detection of breast cancer, where the artifact signal from the breast surface often causes severe interference when focusing on the tumor [1], [2]. While various radar imagery algorithms based on aperture synthesis [3], [4], time reversal approach [5], [6], range migration [7], [8] and numerical solutions for domain integral equations [9] have been developed, they are inappropriate for the above applications because it is generally difficult to achieve simultaneously both low computation cost and high spatial resolution. To address this problem of the conventional techniques, we have already proposed a number of

radar imaging algorithms based on spatial domain interferometry, which accomplish real-time and high resolution surface extraction beyond the pulse width [10], [11]. Although these algorithms have been applied to surface imaging, such as in breast cancer detection [2], through-the-wall imaging [12] or human activity recognition [13], they are actually applicable only for a single object with a simple shape, such as a convex object. As an accurate imaging algorithm with lower computational cost suitable for complex-shaped or multiple targets, the range points migration (RPM) algorithm has been established [14], [15]. This algorithm directly estimates an accurate direction of arrival (DOA) by employing the wider-scale distribution of range points (a set of antenna locations and observed ranges) and avoiding the difficulty of connecting them. However, the RPM or other algorithms have an inherent problem, the aperture size strictly constrains the imaging range of the target boundary. In most cases, the greater part of a target shape, such as its side, falls into a shadow region, that is defined as the area being not reconstructed by single scattered components.

To resolve this difficulty and enhance the imaging range, the SAR algorithm considering a double scattered path has been developed [16]. Although this algorithm demonstrates that shadow region imaging is possible by positively using double scattered signals without preliminary observations or target models, which are required in other algorithms [17]–[19], it requires multiple integrations of the received signals. As a fast and non-parametric imaging approach for this issue, our former algorithm described in [20] successfully expands the imaging region with low computational cost, by combining the RPM algorithm and the original relationship between the range derivatives and each DOA from double scattering centers. However, in the case of complex shapes or noisy situations, it suffers from image degradation caused by situations subject to severe interference due to single and double scattered components or random noises, which can bring out the inaccuracy of derivative operations.

As a solution to this problem, this paper introduces a shadow region imaging algorithm that is based on an advanced RPM principle applied to the double scattered range points distribution. A notable advantage of this algorithm is that it employs the expansive feature of the observed range points to the double scattered centers, instead of employing derivative operations. The principle of this algorithm is similar to that of the original RPM algorithm in that a double scattering point exists on an ellipse whose foci are the an-

Manuscript received July 31, 2012.

Manuscript revised November 7, 2012.

[†]The authors are with the Graduate School of Informatics and Engineering, The University of Electro-Communications, Chofushi, 182-8585 Japan.

a) E-mail: kidera@ee.uec.ac.jp

DOI: 10.1587/transcom.E96.B.1061

tenna location and first scattering point and the major radius is the observed range, and this is regarded as the extension of spatial interferometry to double scattered waves. Furthermore, this algorithm positively employs the normal vector at the first scattering point, which is directly calculated by RPM without using a spatial derivative, and optimizes the first scattering point based on an evaluation function that considers the scattering conditions of the double scattering mechanism. The sequential results of numerical simulations described in Sect. 5 show that the proposed algorithm distinctly enhances the application range of target shapes including complex-shaped or multiple targets, and that there is a non-marginal improvement, particularly in noisy situations, which cannot be accomplished by the conventional algorithms.

2. System Model

Figure 1 shows the system model. The model assumes a mono-static radar and that an omni-directional antenna scans along the x -axis. A static target with arbitrary shape is assumed, and the spatial gradient of conductivity or permittivity along its boundary is expressed as Dirac's delta function [10], the so called clear boundary. The propagation speed of the radio wave c is assumed to be a known constant. A transverse electric (TE) mode wave and cylindrical wave propagation are considered. A mono-cycle pulse with a central wavelength denoted as λ is used as the transmitting current. The real space in which the target and antenna are located is expressed by the parameters (x, z) . $z > 0$ is assumed for simplicity.

Here, $s'(X, t)$ is defined as the electric field received at antenna location $(x, z) = (X, 0)$ at time t . $\tilde{s}(X, t)$ is calculated by applying the Wiener filter to $s'(X, t)$, which is an optimal mean square error (MSE) linear filter for additive noise [14]. $\tilde{s}(X, t)$ is now converted to $s(X, R)$ using the conversion $R = ct/2$, which can be regarded as range profiles. The range points that are candidates for single and double scattered echoes are denoted (X, R_S) and (X, R_D) as shown in Fig. 1, and they are extracted from the local maxima and minima of $s(X, R)$, respectively, that are indicated in the following equations. First, (X, R_S) is extracted as,

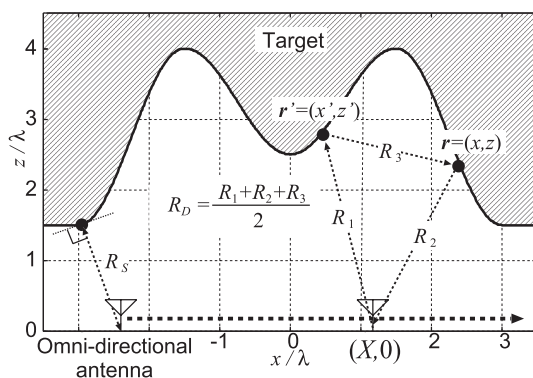


Fig. 1 System model.

$$\left. \begin{aligned} \partial s(X, R) / \partial R &= 0 \\ s(X, R) &\geq \alpha \max_{(X, R)} s(X, R) \end{aligned} \right\}, \quad (1)$$

where $\alpha \geq 0$ is empirically determined. In general, the doubly scattered signal has an anti-phase relationship with the single scattered signal [16], and the negative peaks of $s(X, R)$ are mostly regarded as doubly scattering echoes. (X, R_D) is then defined as the range point of a double scattered wave, which is extracted from the local minimum of $s(X, R)$.

$$\left. \begin{aligned} \partial s(X, R) / \partial R &= 0 \\ s(X, R) &\leq \beta \min_{(X, R)} s(X, R) \end{aligned} \right\}, \quad (2)$$

where $\beta \geq 0$ is also empirically determined. Note that the values of α and β used in Eqs. (1) and (2) relate to the reliability of extracting single and double scattering signals. To avoid the extraction of false ranges generated by random noise or sidelobe effects, these values should not be too small. In contrast, to obtain the certain number of the actual range points, they should not be too large. Furthermore, the above extracted range points naturally include triple or higher multiple scattering components, the amplitudes of which are generally smaller than those of the single or double scattering signals.

3. Conventional Algorithm

This section introduces two typical conventional algorithms proactively employing double scattered components for image expansion, for comparison with the proposed algorithm. One is SAR based extension algorithm to double scattered signals [16]. The other algorithm exploits the range derivative of double scattered range points to achieve fast shadow region imaging, where an inherent characteristic of RPM using single scattered wave [14] is well combined.

3.1 SAR Based Algorithm

SAR employing the double scattered signal has been developed to enhance the imaging range, including in the shadow region [16], defined as the area that cannot be reconstructed by single scattered signals. Here, the same system and signal models are used as in Sect. 2. In general, a double scattered wave propagates along a path different from that of a single scattered wave. It therefore often provides independent information of the two scattering points. This algorithm calculates the image using double scattered waves as $I_2(\mathbf{r})$,

$$I_2(\mathbf{r}) = - \int_{\mathbf{r}' \in \mathbf{R}} \int_{X \in \Gamma} I_1(\mathbf{r}') s(X, d_2(\mathbf{r}, \mathbf{r}', X)/2) dX d\mathbf{r}', \quad (3)$$

where $\mathbf{r}' = (x', z')$, \mathbf{R} denotes the region of real space, $s(X, *)$ is the output of the Wiener filter, and $d_2(\mathbf{r}, \mathbf{r}', X) = \sqrt{(x - X)^2 + z^2} + \sqrt{(x' - X)^2 + z'^2} + \sqrt{(x - x')^2 + (z - z')^2}$. The minus sign in Eq. (3) creates a positive image focused by double scattered waves that have an antiphase relationship with a single scattered wave. Here, the initial image $I_1(\mathbf{r})$ is defined as the original SAR image:

$$I_1(\mathbf{r}) = \int_{X \in \Gamma} s(X, d_2(\mathbf{r}, \mathbf{r}, X)/2) dX, \quad (4)$$

Equation (3), which is a simple expression of the aperture synthesis of the received signals that considers a double scattered path, can be regarded as a coherent integration scheme because $I_1(\mathbf{r})$ denotes the amplitude and its positive outputs offer the target boundary. Any extension of the SAR algorithm, such as an omega-k migration [4] range-Doppler algorithm, can be used in creating $I_1(\mathbf{r})$. The final image is expressed as

$$I'(\mathbf{r}) = \frac{I_1(\mathbf{r})H(I_1(\mathbf{r}))}{\max_r I_1(\mathbf{r})} + \frac{I_2(\mathbf{r})H(I_2(\mathbf{r}))}{\max_r I_2(\mathbf{r})}, \quad (5)$$

where $H(*)$ is the Heaviside function.

A notable feature of this algorithm is that it can reproduce the shadow region employing the double scattered signals, without using target modeling or *a priori* knowledge of the surroundings. However, it requires multiple integrations for each image pixel and has a high calculation cost. Furthermore, a more detailed target structure, such as clear surfaces or edges, are hardly identified employing this algorithm, because the produced image is basically blurred due to the insufficient spatial resolution limited by the frequency bandwidth of the transmitted signal.

3.2 Range Derivative Based Algorithm

As a fast approach for imaging shadow regions, we have already developed the range derivative based algorithm, which employs target points preliminarily created employing the RPM algorithm. It directly reconstructs the target points corresponding to the double scattered signals, where each derivative of their range points is employed. Here, two target points originating from doubly scattering are defined as $\mathbf{p}_1 = (x_1, z_1)$ and $\mathbf{p}_2 = (x_2, z_2)$, respectively. $\mathbf{p}_L = (X, 0)$ denotes an antenna location. This algorithm employs the relationship,

$$\frac{\partial R_D}{\partial X} = -\frac{(\cos \theta_1 + \cos \theta_2)}{2}, \quad (6)$$

where $\theta_1 = \cos^{-1}((x_1 - X)/R_1)$, $\theta_2 = \cos^{-1}((x_2 - X)/R_2)$, $R_1 = \|\mathbf{p}_1 - \mathbf{p}_L\|$ and $R_2 = \|\mathbf{p}_2 - \mathbf{p}_L\|$ are defined. Once \mathbf{p}_1 is determined, θ_2 is directly calculated using Eq. (6) with $\partial R_D / \partial X$. Besides, if the normal vector \mathbf{e}_n on \mathbf{p}_1 is given, the law of reflection derives $R_2 = R_D - R_1 \frac{(R_D - R_1)(\mathbf{e}_1 \cdot \mathbf{e}_n)^2}{R_D - R_1(\mathbf{e}_1 \cdot \mathbf{e}_n)^2}$, where $\mathbf{e}_1 = (\mathbf{p}_1 - \mathbf{p}_L)/R_1$ holds. Namely, \mathbf{p}_2 can be calculated from \mathbf{p}_1 and \mathbf{e}_n with $\partial R_D / \partial X$. Furthermore, \mathbf{p}_2 satisfies $\mathbf{p}_2 = \mathbf{p}_1 + R_3 \mathbf{e}_3$, where $R_3 = \|\mathbf{p}_2 - \mathbf{p}_1\| = 2R_D - R_1 - R_2$ and $\mathbf{e}_3 = \mathbf{e}_1 - 2(\mathbf{e}_n \cdot \mathbf{e}_1)\mathbf{e}_n$. Figure 2 shows the relationship among the scattered points \mathbf{p}_1 , \mathbf{p}_2 and the antenna location \mathbf{p}_L .

In addition, this algorithm employs the initial target points derived by RPM as the first scattering location \mathbf{p}_1 with its normal vector \mathbf{e}_n . In addition, each normal vector $\mathbf{e}_{n,i}^{\text{rpm}}$ on $\mathbf{p}_i^{\text{rpm}}$ is given as $\mathbf{e}_{n,i}^{\text{rpm}} = (X_i^{\text{rpm}} - x_i^{\text{rpm}}, -z_i^{\text{rpm}})/R_i^{\text{rpm}}$, which is given by the direction of the line of sight from the

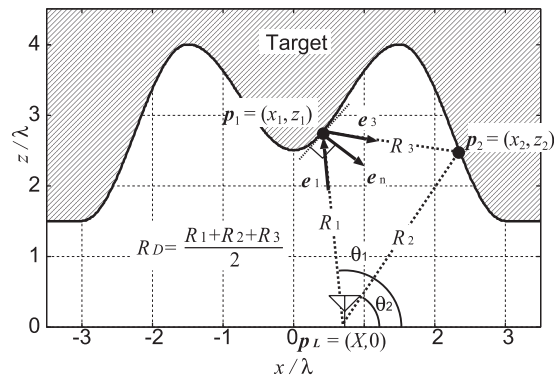


Fig. 2 Relationship between the first and second scattering centers as \mathbf{p}_1 and \mathbf{p}_2 , and their DOAs as θ_1 and θ_2 .

antenna location [14]. Here, $\mathbf{Q}_i = (X_i, R_{D,i})$, ($i = 0, \dots, N_Q$) and $\mathbf{P}_j = (\mathbf{p}_j^{\text{rpm}}, \mathbf{e}_{n,j}^{\text{rpm}})$, ($j = 0, \dots, N_{\text{rpm}}$) are defined, where N_Q and N_{rpm} denote the numbers of (X, R_D) and the target points obtained by RPM. This algorithm determines an optimal \mathbf{P} for \mathbf{Q}_i using numerically calculated $\partial R_{D,i} / \partial X_i$ as,

$$\tilde{\mathbf{P}}(\mathbf{Q}_i) = \arg \min_{\mathbf{P}_j \in \mathcal{P}_{\text{rpm}}} \left\| \mathbf{p}_2^A(\mathbf{Q}_i; \mathbf{P}_j) - \mathbf{p}_2^B\left(\mathbf{Q}_i, \frac{\partial R_{D,i}}{\partial X_i}; \mathbf{P}_j\right) \right\|, \quad (7)$$

where \mathcal{P}_{rpm} is a set of \mathbf{P}_j , and

$$\begin{aligned} \mathbf{p}_2^A(\mathbf{Q}_i; \mathbf{P}_j) &= \mathbf{p}_j^{\text{rpm}} + R_3(\mathbf{Q}_i; \mathbf{P}_j)\mathbf{e}_3(\mathbf{Q}_i; \mathbf{P}_j), \\ \mathbf{p}_2^B(\mathbf{Q}_i, \partial R_{D,i} / \partial X_i; \mathbf{P}_j) &= \mathbf{p}_{L,i} + R_2(\mathbf{Q}_i; \mathbf{P}_j) \\ &\times \left(\cos \theta_2 \left(\mathbf{Q}_i, \frac{\partial R_{D,i}}{\partial X_i}; \mathbf{P}_j \right), \sin \theta_2 \left(\mathbf{Q}_i, \frac{\partial R_{D,i}}{\partial X_i}; \mathbf{P}_j \right) \right), \end{aligned} \quad (8)$$

are given. Then, the optimum second scattering point is determined as

$$\tilde{\mathbf{p}}_2(\mathbf{Q}_i) = \frac{\mathbf{p}_2^A(\mathbf{Q}_i; \tilde{\mathbf{P}}(\mathbf{Q}_i)) + \mathbf{p}_2^B(\mathbf{Q}_i, \partial R_{D,i} / \partial X_i; \tilde{\mathbf{P}}(\mathbf{Q}_i))}{2}.$$

Although this algorithm accomplishes fast imaging without any integration, it requires a derivative operation of the range curves that could enhance small range fluctuations; that is, its accuracy suffers severely in the case of a target with complex-shape or in a noisy situation.

4. Proposed Algorithm

4.1 Basic Theory of the Proposed Algorithm

As a promising solution to the previous difficulties, this paper proposes a novel shadow region imaging algorithm that is not based on range derivatives, but exploits the wider range of the distribution (X, R_D) , which can provide an integral effect for imaging. The algorithm can be regarded as a doubly scattered RPM algorithm. This algorithm employs only the group of $\mathbf{p}_2^A(\mathbf{Q}_i; \mathbf{P}_j)$, which is defined in Eq. (8) without using a derivative operation. The algorithm is also

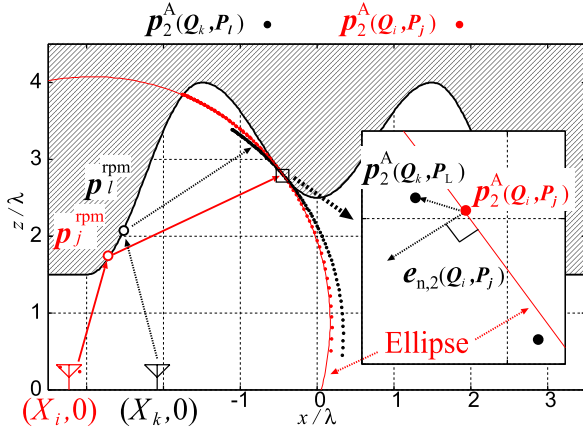


Fig. 3 Relationship among $p_2^A(Q_i; P_j)$, $p_2^A(Q_k; P_l)$ and the ellipse.

combined with the original RPM algorithm to estimate the first scattering center and its normal vector, namely the parameter P_j , defined as in Sect. 3.2. The proposed algorithm is based on the following two principles.

Principle I: If P_j is the actual P , the closest point between $p_2^A(Q_i; P_j)$ and $p_2^A(Q_k; P_l)$ when varying P_l should converge around the actual secondary scattering point when $Q_k \rightarrow Q_i$.

Principle II: The second scattering point p_2 exists on an ellipse whose foci are p_1 and p_L , and whose major diameter is $|2R_D - R_1|$, and this ellipse must be tangent to the target boundary at the second scattering point according to the law of reflection.

Principle I is analogous to the principle of spatial domain interferometry, where the effect of the scattering center shift along the target boundary in terms of antenna location is considered. Principle II can be regarded as the stationary phase condition in propagating along the double scattered path. Figure 3 illustrates the relationship among $p_2^A(Q_i; P_j)$, $p_2^A(Q_k; P_l)$ and the above ellipse.

Following the two principles, the algorithm calculates the optimum first scattering parameter $\hat{P}(Q_i)$ as

$$\hat{P}(Q_i) = \arg \max_{P_j \in \mathcal{P}_{\text{rpm}}} \sum_{k=1}^{N_Q} s(Q_k) \exp\left(-\frac{|X_i - X_k|^2}{2\sigma_X^2}\right) \times \exp\left(-\frac{\left| \left(p_2^A(Q_i; P_j) - p_2^A(Q_k; P_L) \right) \cdot e_{n,2}(Q_i; P_j) \right|^2}{2\sigma_p^2}\right), \quad (10)$$

where σ_X and σ_p are empirically determined constants. $e_{n,2}(Q_i; P_j)$ denotes the normal vector at $p_2^A(Q_i; P_j)$, which is determined by p_j^{rpm} and $p_{L,i}$ according to the law of reflection as shown in Fig. 3. The term $\exp\left(-\frac{|X_i - X_k|^2}{2\sigma_X^2}\right)$ in Eq. (10) is a measure of the degree of convergence in terms of antenna location, as described by Principle I, which is

similar to the principle used in the original RPM [14]. In addition, the last weighting term in Eq. (10) assesses Principle II; that is, the distance from the ellipse tangent to the target boundary, which is evaluated as the absolute value of the inner product of $p_2^A(Q_i; P_j) - p_2^A(Q_k; P_L)$ and $e_{n,2}(Q_i; P_j)$. P_L is defined as

$$P_L = \arg \min_{P_l \in \mathcal{P}_{\text{rpm}}} \left\| p_2^A(Q_i; P_j) - p_2^A(Q_k; P_l) \right\|. \quad (11)$$

Finally, the second scattering point \hat{p}_2 for Q_i is calculated as

$$\hat{p}_2(Q_i) = p_2^A(Q_i; \hat{P}(Q_i)). \quad (12)$$

This algorithm does not require the derivative operation for imaging the shadow region, and is less sensitive to small range fluctuations due to random components or interference echoes from other scattering locations.

4.2 Procedure of the Proposed Algorithm

The actual procedure of the proposed algorithm is summarized as follows.

Step 1). Range points for single and double scattered signals are extracted as $(X_j, R_{S,j})$ and $(X_i, R_{D,i})$ from $s(X, R)$ using Eqs. (1) and (2).

Step 2). A set of target points $\mathcal{T}_{\text{rpm}} = \{p_j^{\text{rpm}}, (j = 1, \dots, N_{\text{rpm}})\}$ is obtained by applying RPM to $(X_j, R_{S,j})$, and the set of parameter vectors $P_j = (p_j^{\text{rpm}}, e_{n,j}^{\text{rpm}})$ is determined.

Step 3). For each $Q_i = (X_i, R_{D,i})$, $\hat{P}(Q_i)$ is calculated using Eq. (10).

Step 4). For the optimal $\hat{P}(Q_i)$, the condition,

$$\zeta(\hat{P}(Q_i)) \geq \max_{Q_i} \gamma \zeta(\hat{P}(Q_i)), \quad (13)$$

is investigated, where $\zeta(*)$ denotes the evaluation function described by the right term in Eq. (10). If Eq. (13) is satisfied, $\hat{p}_2(Q_i)$ is calculated using Eq. (12) with $\hat{P}(Q_i)$, and it is added to the set of target points as \mathcal{T}_D .

Step 5). Steps 3) and 4) are repeated for all range points Q_i .

Step 6). The final set of target points is obtained as $\mathcal{T} = \mathcal{T}_{\text{rpm}} \cup \mathcal{T}_D$.

Step 4) prevents the occurrence of false images attributed to random noise, because the evaluation function $\zeta(*)$ for noisy range point insufficiently grows in the case that the range points are randomly distributed in the data space as (X, R_D) .

5. Performance Evaluation in Numerical Simulation

This section presents numerical examples of the use of the

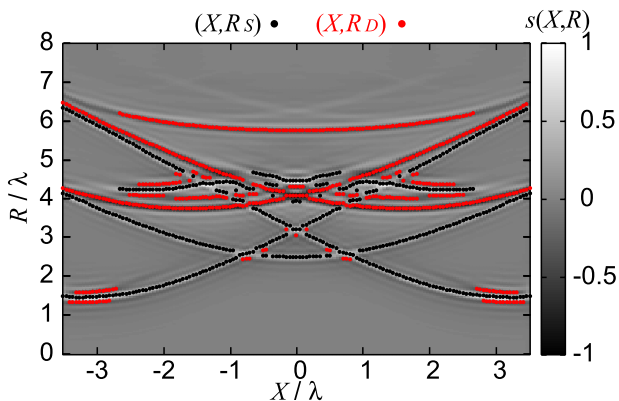


Fig. 4 Output of Wiener filter and extracted range points (X, R_S) and (X, R_D) in the case of Fig. 1.

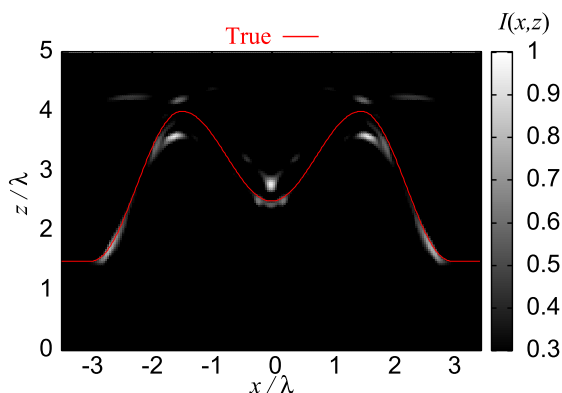


Fig. 5 Image obtained by the conventional SAR-based algorithm.

algorithms described above. Figure 4 shows the output of the Wiener filter and each of the extracted range points (X, R_S) and (X, R_D) , where the target boundary is assumed to be the same as in Fig. 1. Note that the space expressed in Fig. 4 (conventionally referred to as data space) is totally different from the actual space (x, z) . $\alpha = 0.3$ and $\beta = 0.3$ are set in Eqs. (1) and (2). A noiseless situation is assumed here. The received signals are calculated at 141 locations for $-3.5\lambda \leq x \leq 3.5\lambda$ using finite difference time domain (FDTD) method, which can strictly calculate a realistic electromagnetic field including a multiple scattering or a frequency dependency in scattering phenomena [15]. Figure 5 illustrates the image obtained by the SAR-based conventional algorithm described in Sect. 3.1. This figure shows that while the image can be expanded to the concave area, there are many undesirable responses far from the actual target boundary. This is because this algorithm simply synthesizes the output's waveform along the double scattered paths, and then tends to produce false images owing to the range sidelobe of filter responses or other interference components from multiple scattering centers. Figure 6 presents the target points estimated using the RPM [14] corresponding to single scattered signal migration and the conventional range derivative based (RD-based) algorithms [20], and indicates that the estimated target points around

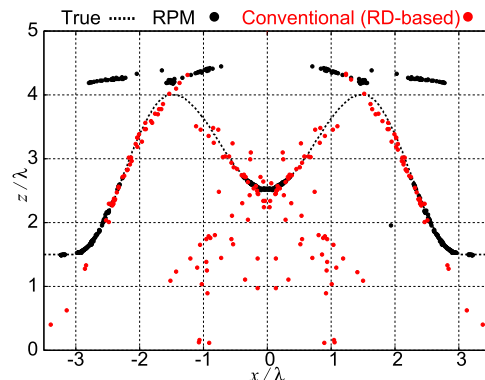


Fig. 6 Image obtained by the conventional RD-based algorithm.

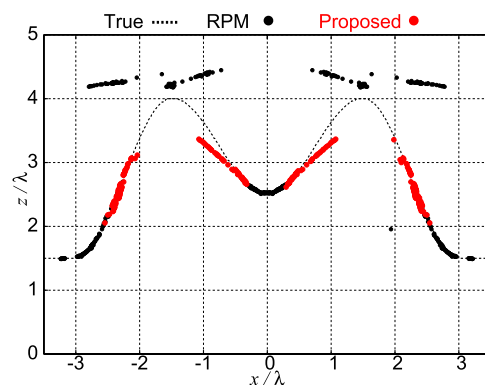


Fig. 7 Image obtained by the proposed algorithm.

the convex boundary are far from the actual boundary; i.e., there is serious accuracy degradation. This is because each range derivative suffers from inaccuracy caused by richly interfered signals, particularly in the region $|X| \leq 2.0\lambda$ and $3.0\lambda \leq R \leq 5.0\lambda$ in Fig. 4. By contrast, Fig. 7 shows the target points obtained using the proposed algorithm, for which the same data as in Fig. 4 are used. $\sigma_p = 0.05\lambda$ and $\sigma_x = 1.0\lambda$ are set. Obviously, this algorithm produces only accurate target points, because it employs a more expansive distribution of range points (X, R_D) , which can suppress image distortion due to small range fluctuations. Naturally, both the images obtained with the RPM and the proposed algorithm are useful for object recognition. As an important remark, any method including the proposed method cannot reconstruct the concave area of the target boundary as in Fig. 7, because a sufficient echo for either single or double scattering cannot be obtained at any antenna location. Note that RPM produces false images over the actual boundary because of components relating to triple or higher scattering. However, such false images originate from single scattered signal migration schemes such as RPM, and can be suppressed by approaches such as those described in [10] and [16].

Furthermore, examples of noisy situations are investigated. White Gaussian noise is added to each received signal as $s'(X, R)$. First, we investigate the higher S/N case. Figures 8 and 9 are images obtained by the conventional

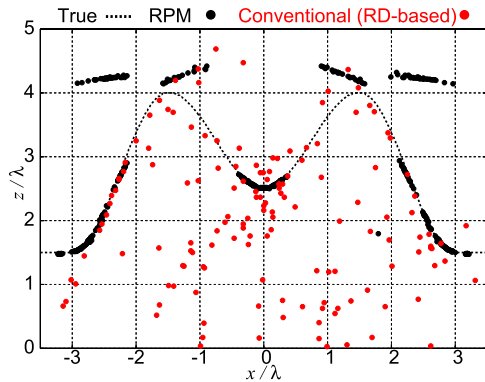


Fig. 8 Image obtained by the conventional RD-based algorithm at $S/N=30$ dB.

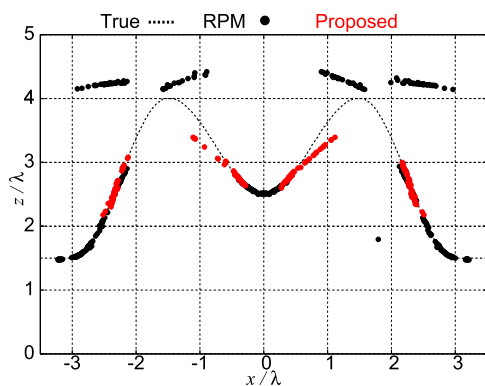


Fig. 9 Image obtained by the proposed algorithm at $S/N=30$ dB.

RD-based and proposed algorithms, respectively, for a mean S/N of 30 dB. S/N is defined as the ratio of the peak signal power to the averaged noise power after applying the matched filter with the transmitted waveform. These figures show that while the conventional RD-based method suffers from severe accuracy degradation caused by noisy components, the level of imaging accuracy offered by the proposed method is the same as that obtained in the noiseless situation. These results demonstrate the effectiveness of the proposed method in terms of robust and accurate shadow region imaging. Next, the lower S/N cases are assessed to evaluate the robustness of each imaging method. Figure 10 presents the output of the Wiener filter and the extracted range points (X, R_S) and (X, R_D) , respectively, where the mean S/N is around 20 dB. In Fig. 10, there are many range points produced by the noisy components, and it is apparently difficult to recognize the actual distribution of range points as shown in Fig. 4. Figures 11 and 12 show the images obtained by the conventional RD-based and proposed algorithms, respectively. These figures clearly illustrate the superiority of the proposed algorithm in terms of insensitivity against the random noises. This superiority mainly originates from the proposed algorithm not employing derivative operation, which is basically sensitive to small fluctuations of the observed ranges, and the false images owing to noises are also eliminated according to the criteria described in Step 4) of

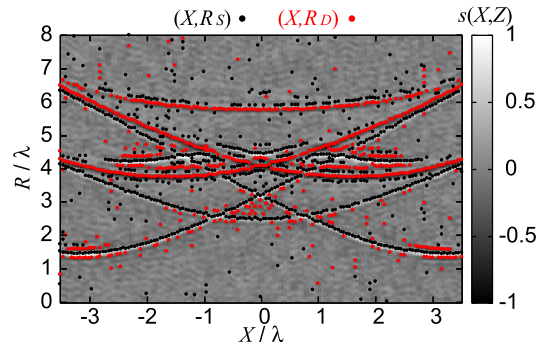


Fig. 10 Output of Wiener filter and extracted range points (X, R_S) and (X, R_D) in the case of Fig. 1 at $S/N=20$ dB.

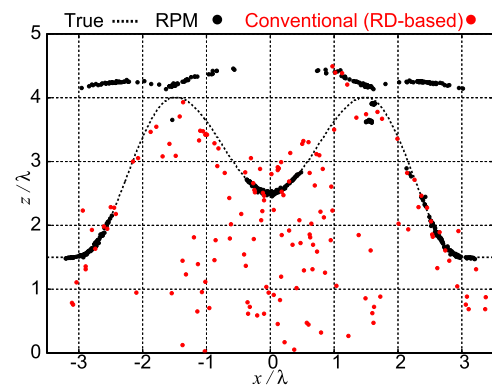


Fig. 11 Image obtained by the conventional RD-based algorithm at $S/N=20$ dB.

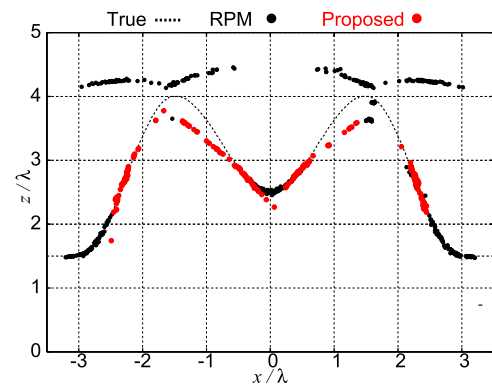


Fig. 12 Image obtained by the proposed algorithm at $S/N=20$ dB.

the proposed algorithm.

Here, the quantitative analysis is introduced using ϵ_i defined as,

$$\epsilon_i = \min_{\mathbf{p}_{\text{true}}} \|\mathbf{p}_{\text{true}} - \mathbf{p}_e^i\|, \quad (i = 1, \dots, N_T), \quad (14)$$

where \mathbf{p}_{true} and \mathbf{p}_e^i express the locations of the true and estimated target points only including the points obtained from the double scattered signals, respectively. N_T is the total number of \mathbf{p}_e^i . Figure 13 plots the number of estimated points for each value of ϵ_i in noiseless and noisy ($S/N=30$ dB and 20 dB) cases. The figure verifies that the proposed algo-

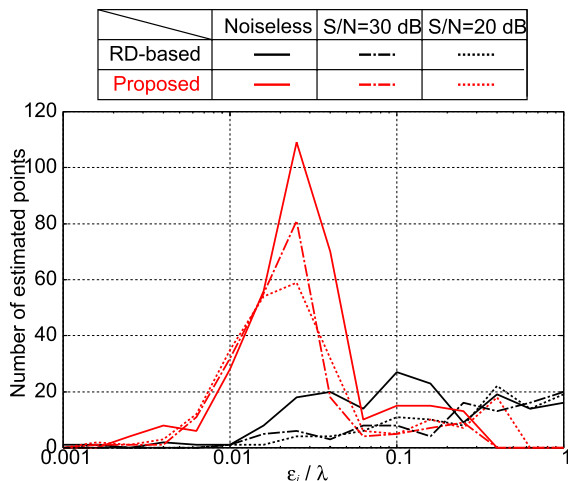


Fig. 13 Number of target points with ϵ_i for each method in noiseless and noisy cases.

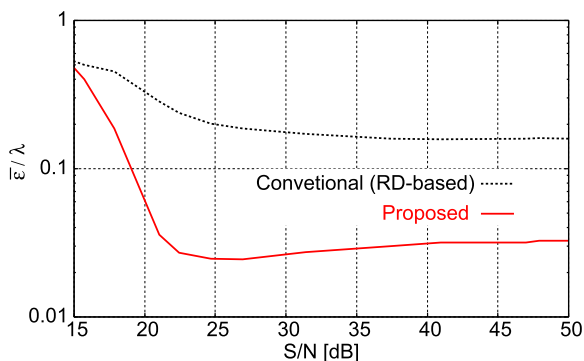


Fig. 14 Mean accuracy versus S/N for each method.

algorithm increases the number of target points with accuracy of around 0.03λ , simultaneously enhancing the imaging range. The mean values of ϵ_i for the conventional RD-based algorithm are 0.22λ in the noiseless case, 0.24λ in S/N=30 dB, and 0.38λ in S/N=20 dB. By contrast, these values for the proposed algorithm are $3.4 \times 10^{-2}\lambda$ in the noiseless case, 2.9×10^{-2} in S/N=30 dB, and 4.9×10^{-2} in S/N=20 dB. Furthermore, the mean accuracy $\bar{\epsilon}$ versus S/N for each algorithm is shown in Fig. 14, in this target case. The number of Monte Carlo trial is 100. The figure reveals a distinct benefit of using the proposed algorithm, from a statistical viewpoint, in that if S/N is greater than 20 dB, the algorithm has accuracy around 0.03λ , which is about 10 times better than that achieved using the conventional RD-based algorithm.

To investigate the relevance of the proposed algorithm, another target case, where multiple ellipse targets are assumed, is investigated. Figure 15 shows the output of the Wiener filter and both extracted range points, where three elliptical targets are assumed and the mean S/N is approximately 20 dB. In this figure, we also face the difficulty of connecting the range points, which worsen the accuracy of the derivative calculation. Figures 16 and 17 illustrate the estimated images obtained by the SAR-based and RD-based

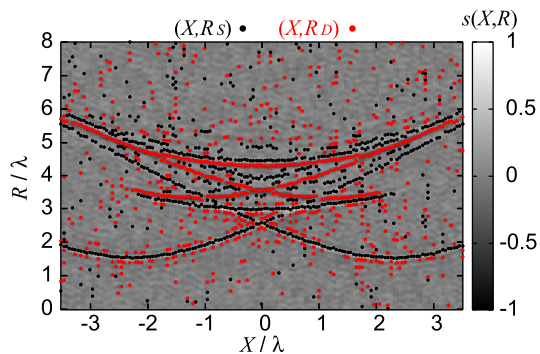


Fig. 15 Output of Wiener filter and extracted range points (X, R_S) and (X, R_D) in the case of three ellipse targets at S/N=20 dB.

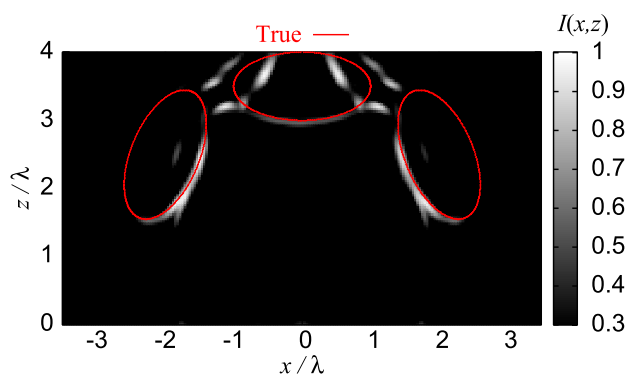


Fig. 16 Image obtained by the conventional SAR-based algorithm in the case of three ellipse targets at S/N=20 dB.

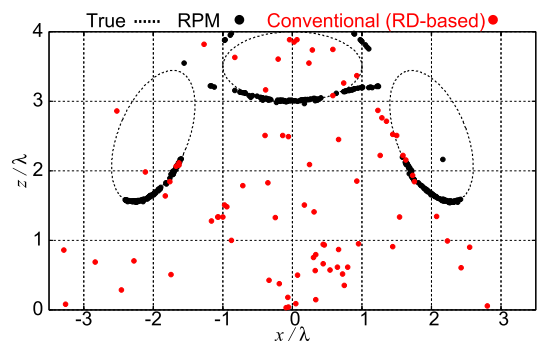


Fig. 17 Image obtained by the conventional RD-based algorithm in the case of three ellipse targets at S/N=20 dB.

algorithms as conventional algorithms, respectively. Both results show serious image degradations caused by the complicated situations in terms of the received signals or range points distributions due to the same reason described in the previous case. On the other hand, Fig. 18 presents the estimated image reproduced by the proposed algorithm. These figures clearly illustrate the superiority of the proposed algorithm in terms of stability of the algorithm against the random noise or interference, and the side of the ellipse is accurately reproduced in such noisy and high interference situations. Finally, Fig. 19 presents the statistical and quantitative evaluation for this target case, giving the mean accuracy

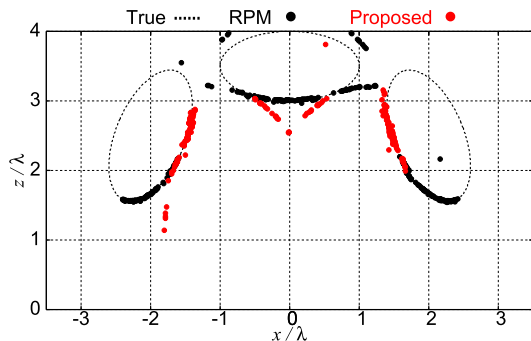


Fig. 18 Image obtained by the proposed algorithm in the case of three ellipse targets at $S/N=20$ dB.

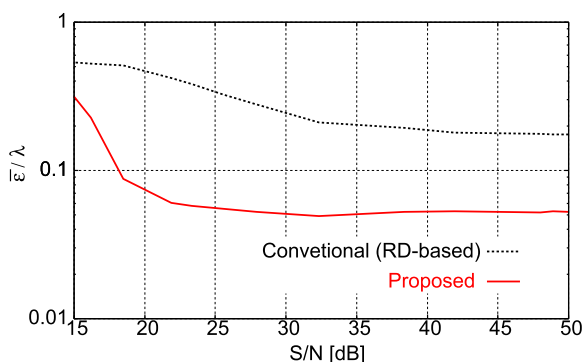


Fig. 19 Mean accuracy versus S/N for each method in the case of three ellipse targets.

$\bar{\epsilon}$ versus S/N . The figure also verifies the effectiveness of the proposed algorithm in that the accuracy is remarkably enhanced from that obtained with the conventional RD-based algorithm.

Finally, the computational complexity of each algorithm is investigated. The conventional SAR-based algorithm has computational complexity of around $O(N_X N_x^2 N_z^2)$, where N_X , N_x and N_z denote the sampling numbers for the antenna location X , and the spatial coordinates x and z , respectively, and $O(*)$ is Landau notation. This is because the conventional SAR-based algorithm should employ the triple integration for each image pixel as in Eq. (3). On the other hand, the RD-based algorithm has computational complexity of around $O(N_X^2)$, since it requires only a searching operation for the first scattering points obtained by RPM ($O(N_X)$) for each range point ($O(N_X)$). The computational complexity of the proposed algorithm is estimated as $O(N_X^3)$, because it requires the two searching operation depending on the number of the RPM target points as in Eqs. (10) and (11) ($O(N_X^2)$) for each range point ($O(N_X)$). Table 1 compares the computational times when using an Intel Pentium D 2.8 GHz processor with 800 MB memory, and the computational complexity for each algorithm. In this case, $N_X = N_x = 141$ and $N_z = 71$, where each pixel size is 0.05λ . The computational times of the SAR-based, the RD-based and the proposed algorithms are 2×10^3 sec, 1.0 sec, 20 sec, respectively. The table shows that the computation

Table 1 Calculation time (for Intel Pentium D 2.8 GHz processor) and computer complexity of each algorithm.

	Calculation time	Computational complexity
SAR-based	2.0×10^3 sec	$O(N_X N_x^2 N_z^2)$
RD-based	1.0 sec	$O(N_X^2)$
Proposed	20 sec	$O(N_X^3)$

cost of the proposed algorithm is 100 times less than that of the conventional SAR-based algorithm. While the proposed algorithm has 20 times the calculation cost of the RD-based algorithm, it has the substantial advantage of accuracy and robustness even in severe situations, investigated in this paper.

6. Conclusion

This paper proposed a novel accurate and robust shadow region imaging algorithm, advancing the RPM principle to doubly scattered signals. Our method dispenses with the derivative operation, which is sensitive to small range fluctuations, and instead focuses on the extensive distribution of the doubly scattered range points, by extending the basis of the spatial interferometry approach and incorporating the phase stationary condition of the double scattered waves. Numerical examples, including complex-shaped or multiple objects cases, showed that the proposed method had accuracy of the order of $1/100 \lambda$, even in interference-rich environments, which is impossible with conventional SAR-based or range derivative based algorithms. In more noisy situations, the statistical and quantitative analyses demonstrated that the proposed algorithm produced an accurate image of the shadow region by suppressing the small range fluctuations. The proposed method can thus be applied to actual radar applications such as robotic or security sensors. Note that, as mentioned in Sect. 5, no method necessarily reproduces the whole the target boundary, especially for the deep concave area or target side. Thus, we will carry out important future work to expand the reconstructible area by exploiting triple or higher-order multiple scattering components or by adjusting the scanning orbit of the antenna to obtain the echoes of single or double scattering at a significant level.

Acknowledgment

This work is supported in part by the Grant-in-Aid for Scientific Research (B) (Grant No. 22360161), the Grant-in-Aid for Young Scientists (B) (Grant No. 23760364), promoted by Japan Society for the Promotion of Science (JSPS), the Research Grant promoted by CASIO Science Promotion Foundation.

References

- [1] T.C. Williams, J.M. Sill, and E.C. Fear, "Breast surface estimation for radar-based breast imaging system," *IEEE Trans. Biomed. Eng.*, vol.55, no.6, pp.1678–1686, June 2008.

- [2] D.W. Winters, J.D. Shea, E.L. Madsen, G.R. Frank, B.D. Van Veen, and S.C. Hagness, "Estimating the breast surface using UWB microwave monostatic backscatterer measurements," *IEEE Trans. Biomed. Eng.*, vol.55, no.1, pp.247–256, Jan. 2008.
- [3] D.L. Mensa, G. Heidbreder, and G. Wade, "Aperture synthesis by object rotation in coherent imaging," *IEEE Trans. Nucl. Sci.*, vol.27, no.2, pp.989–998, April 1980.
- [4] X. Xu, E.L. Miller, and C.M. Rappaport, "Minimum entropy regularization in frequency-wavenumber migration to localize subsurface objects," *IEEE Trans. Geosci. Remote Sens.*, vol.41, no.8, pp.1804–1812, Aug. 2003.
- [5] D. Liu, G. Kang, L. Li, Y. Chen, S. Vasudevan, W. Joines, Q.H. Liu, J. Krolik, and L. Carin, "Electromagnetic time-reversal imaging of a target in a cluttered environment," *IEEE Trans. Antennas Propag.*, vol.53, no.9, pp.3058–3066, Sept. 2005.
- [6] D. Liu, J. Krolik, and L. Carin, "Electromagnetic target detection in uncertain media: Time-reversal and minimum-variance algorithms," *IEEE Trans. Geosci. Remote Sens.*, vol.45, no.4, pp.934–944, April 2007.
- [7] J. Song, Q.H. Liu, P. Torrione, and L. Collins, "Two-dimensional and three dimensional NUFFT migration method for landmine detection using ground-penetrating radar," *IEEE Trans. Geosci. Remote Sens.*, vol.44, no.6, pp.1462–1469, June 2006.
- [8] F. Soldovieri, A. Brancaccio, G. Prisco, G. Leone, and R. Pieri, "A Kirchhoff-based shape reconstruction algorithm for the multimono-static configuration: The realistic case of buried pipes," *IEEE Trans. Geosci. Remote Sens.*, vol.46, no.10, pp.3031–3038, Oct. 2008.
- [9] A. Massa, D. Franceschini, G. Franceschini, M. Pastorino, M. Raffetto, and M. Donelli, "Parallel GA-based approach for microwave imaging applications," *IEEE Trans. Antennas Propag.*, vol.53, no.10, pp.3118–3127, Oct. 2005.
- [10] T. Sakamoto and T. Sato, "A target shape estimation algorithm for pulse radar systems based on boundary scattering transform," *IEICE Trans. Commun.*, vol.E87-B, no.5, pp.1357–1365, May 2004.
- [11] S. Kidera, T. Sakamoto, and T. Sato, "High-resolution and real-time UWB radar imaging algorithm with direct waveform compensations," *IEEE Trans. Geosci. Remote Sens.*, vol.46, no.11, pp.3503–3513, Nov. 2008.
- [12] S. Hantscher, A. Reizenhahn, and C.G. Diskus, "Through-wall imaging with a 3-D UWB SAR algorithm," *IEEE Signal Process. Lett.*, vol.15, pp.269–272, Feb. 2008.
- [13] H. Wang, H. Xue, and M. Ge, "Application and practice of system integration approach in intelligent human motion recognition," *Proc. Intl. Conf. on Computer Science and Software Engineering* vol.1, 2008.
- [14] S. Kidera, T. Sakamoto, and T. Sato, "Accurate UWB radar 3-D imaging algorithm for complex boundary without range points connections," *IEEE Trans. Geosci. Remote Sens.*, vol.48, no.4, pp.1993–2004, April 2010.
- [15] S. Kidera, T. Sakamoto, and T. Sato, "Super-resolution UWB radar imaging algorithm based on extended Capon with reference signal optimization," *IEEE Trans. Antennas & Propag.*, vol.59, no.5, pp.1606–1615, May 2011.
- [16] S. Kidera, T. Sakamoto, and T. Sato, "Extended imaging algorithm based on aperture synthesis with double scattered waves for UWB radars," *IEEE Trans. Geosci. Remote Sens.*, vol.49, no.12, pp.5128–5139, Dec. 2011.
- [17] J.M.F. Moura and Y. Jin, "Detection by time reversal: Single antenna," *IEEE Trans. Signal Process.*, vol.55, no.1, pp.187–201, Jan. 2007.
- [18] G. Shi and A. Nehorai, "Cramer-rao bound analysis on multiple scattering in multistatic point-scatterer estimation," *IEEE Trans. Signal Process.*, vol.55, no.6, pp.2840–2850, June 2007.
- [19] S. Fujita, T. Sakamoto, and T. Sato, "2-dimensional accurate imaging with UWB radar using indoor multipath echoes for a target in shadow regions," *IEICE Trans. Commun.*, vol.E94-B, no.8, pp.2366–2374, Aug. 2011.
- [20] S. Kidera and T. Kirimoto, "Fast and shadow region 3-dimensional imaging algorithm with range derivative of doubly scattered signals for UWB radars," *IEEE Trans. Antennas Propag.*, vol.60, no.2, pp.984–996, Feb. 2012.



Shouhei Kidera received his B.E. degree in Electrical and Electronic Engineering from Kyoto University in 2003 and M.I. and Ph.D. degrees in Informatics from Kyoto University in 2005 and 2007, respectively. He is an assistant professor in Graduate School of Informatics and Engineering, University of Electro-Communications, Japan. His current research interest is in advanced signal processing for the near field radar, UWB radar. He is a member of the Institute of Electrical and Electronics Engineering (IEEE) and the Institute of Electrical Engineering of Japan (IEEJ).



Tetsuo Kirimoto received the B.S. and M.S. and Ph.D. degrees in Communication Engineering from Osaka University in 1976, 1978 and 1995, respectively. During 1978–2003 he stayed in Mitsubishi Electric Corp. to study radar signal processing. From 1982 to 1983, he stayed as a visiting scientist at the Remote Sensing Laboratory of the University of Kansas. From 2003 to 2007, he joined the University of Kitakyushu as a Professor. Since 2007, he has been with the University of Electro-Communications, where he is a Professor at the Graduate School of Informatics and Engineering. His current study interests include digital signal processing and its application to various sensor systems. Prof. Kirimoto is a member of the Institute of Electrical and Electronics Engineering (IEEE) and and the SICE (Society of Instrument and Control Engineering) of Japan.